

1 Towards a comprehensive view of dust event from multiple
2 satellite and ground measurements: exemplified by the East
3 Asia May 2017 dust storm

4 Lu She^{1,3,4,5}, Yong Xue^{2,3}, Jie Guang³, Yaihui Che³, Cheng Fan³, Ying Li³, Yanqing
5 Xie³

6 ¹College of Resources and Environmental Science, Ningxia University, Ningxia 750021, Ningxia
7 Province, China

8 ²Department of Electronics, Computing and Mathematics, College of Engineering and Technology,
9 University of Derby, Derby DE22 1GB, UK

10 ³Key Laboratory of Digital Earth Science, Institute of Remote Sensing and Digital Earth, Chinese
11 Academy of Sciences, Beijing 100094, China

12 ⁴Ningxia Key Laboratory of Resources Assessment and Environmental Regulation in Arid Regions,
13 Yinchuan 750021, Ningxia Province, China

14 ⁵China-Arab Joint International Research Laboratory for Featured Resources and Environmental
15 Governance in Arid Regions, Yinchuan 750021, Ningxia Province, China.

16

17 *Correspondence to:* Professor Yong Xue (y.xue@derby.ac.uk)

18 **Abstract.** One or several aspects of the source, distribution, transport, optical properties of airborne dust
19 have been characterized using different types of satellite and ground measurements each with unique
20 advantages. In this study, a dust event occurred over the East Asia area in May 2017 was exemplified to
21 demonstrate how all the above mentioned aspects of a dust event can be pictured by combining the
22 advantages of different satellite and ground measurements. The used data included the Himawari-8
23 satellite Advanced Himawari Imager (AHI) true-colour images, the Cloud-Aerosol Lidar and Infrared
24 Pathfinder Satellite Observation (CALIPSO) Cloud-Aerosol Lidar with Orthogonal Polarization
25 (CALIOP) aerosol vertical profiles, the Aura satellite Ozone Monitoring Instrument (OMI) aerosol index
26 images, and the ground based Aerosol Robotic Network (AERONET) aerosol properties and the ground
27 station particulate matter (PM) measurements. From the multi-satellite/sensor (AHI, CALIOP and OMI)
28 time series observations, the dust storm was found to originate from the Gobi Desert on the morning of
29 3 May 2017 and transport northeastward to the Bering Sea, eastward to the Korean Peninsula and Japan,
30 and southward to south-central China. The air quality in China deteriorated drastically: the PM₁₀ (PM<10
31 μm in aerodynamic diameter) concentrations measured at some air quality stations located in northern
32 China reached 4333 μg/m³. At the AOE_Baotou, Beijing, Xuzhou-CUMT, and Ussuriysk AERONET

33 sites, the maximum aerosol optical depth values reached 2.96, 2.13, 2.87, and 0.65 and the extinction
34 Ångström exponent dropped to 0.023, 0.068, 0.03, and 0.097, respectively. The dust storm also induced
35 unusual aerosol spectral single-scattering albedo and volume size distribution.

36 **1. Introduction**

37 Large amounts of dust particles are emitted from the deserts in western/northern China and southern
38 Mongolia every year, especially in spring (Shao et al., 2011). The annual dust emissions of eastern Asia
39 reach approximately 25% of the total global dust emissions (Ginoux et al., 2004). These massive
40 emissions produce significant influences on the Earth's radiation balance, climate, ambient air quality
41 and human health (Goudie, 2009;Shao et al., 2011;Rodríguez et al., 2012). Dust aerosols exert both direct
42 and indirect effects on the climate system. Dust can directly scatter and absorb solar radiation over
43 ultraviolet, visible, and infrared wavelengths, resulting in positive or negative forcing (Rosenfeld et al.,
44 2001;Tegen, 2003). Dust is also involved in cloud formation and precipitation processes and can alter
45 the albedo of snow and ice surfaces, thereby causing indirect effects on the Earth's energy budget
46 (Rodríguez et al., 2012;Rosenfeld et al., 2001;Bangert et al., 2012).

47 Due to the long-distance transport of dust plumes (Zhu et al., 2007), dust particles can alter the
48 atmospheric conditions in regional even global scale(Goudie, 2009). The dust aerosols from the
49 Taklimakan and Gobi Deserts can travel thousands of miles, thereby affecting large areas of China (Wang
50 et al., 2013;Lee et al., 2010;Chen et al., 2015;Tan et al., 2012), South Korean and Japan (Mikami et al.,
51 2006), and even the Northern Pacific Ocean and North America (Fairlie et al., 2007;Creamean and
52 Prather, 2013;Guo et al., 2017). Dust storms can cause poor air quality and low visibility and have severe
53 effects on the human health and environment (Goudie, 2009;Lee et al., 2010). Desert dust is the main
54 contributor to aerosol loading and particulate matter (PM) mass concentrations in China during the spring
55 season (Wang et al., 2013). During heavy dust outbreaks, PM₁₀ (PM less than 10 µm in aerodynamic
56 diameter) mass concentrations can even reach 20 exceedances of the internationally recommended limit
57 value in northern China. Moreover, dust particles can interact with anthropogenic pollution and smoke,
58 causing air conditions with greater complexity (Dall'Osto et al., 2010).

59 Many literatures have studied desert dust from different perspectives using different satellite data,
60 ground-based observations and model simulations (Badarinath et al., 2010;Wang et al., 2013;Teixeira et

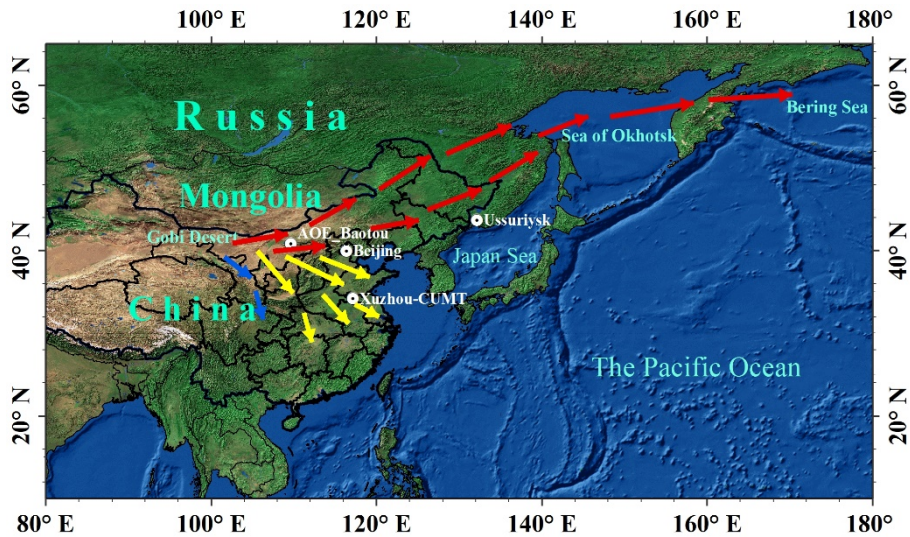
61 al., 2016). For example, some analysed the dust chemical composition and dust radiative effects, i.e.,
62 dust optical and micro-physical properties (Alam et al., 2014;Basha et al., 2015;Srivastava et al., 2014).
63 The other focused on the long-distance transport of dust plumes using satellite observations and/or model
64 simulations (Huang et al., 2008;Guo et al., 2017;Athanasopoulou et al., 2016). However, few studies
65 have been carried out to fully examine the source, distribution, transport, optical properties of the dust
66 storm. This is possibly because each observation system can only characterize one or several aspects of
67 them.

68 This study tried to picture a comprehensive view of dust event using different satellite and ground
69 measurements with a recent heavy dust storm over northern China and southern Mongolia from 3 to 8
70 May 2017 as an example. The dust storm spread with wind across south eastern Russia and even reached
71 the Bering Sea on 7-8 May 2017. Satellite time series observations (the Himawari-8 satellite Advanced
72 Himawari Imager (AHI) true-colour images and the Ozone Monitoring Instrument (OMI) aerosol index
73 (AI) images) were used to capture the dust transport. The OMI AI was also used to provide information
74 about the absorbing aerosol distribution. The Cloud-Aerosol Lidar and Infrared Pathfinder Satellite
75 Observation (CALIPSO) data were used to monitor the dust aerosol type and vertical distribution. The
76 Air Resources Laboratory's HYbrid Single-Particle Lagrangian Integrated Trajectory (HYSPLIT) model
77 was used to generate back trajectories to identify the dust sources. Ground-based measurements from
78 both Aerosol Robotic Network (AERONET) and air quality stations were used to analyse the variations
79 in aerosol properties caused by the dust storm. The connections and correspondences among different
80 observations are briefly analysed.

81 **2. Data and methods**

82 **2.1 General description of the study area**

83 Fig. 1 shows the topography of the study area. The deserts in China and Mongolia, where an abundance
84 of dust events occur, constitute the second-largest dust source in the world. During the spring, the Gobi
85 region is affected by the Mongolian cyclones, which is the main factor to the severe Asian dust storms
86 (Shao et al., 2011).



87
88 **Fig. 1. Study area. The white circles with black point represent four AERONET stations and the arrows show**
89 **the dust transport directions.**

90 **2.2 AHI/Himawari-8**

91 The Himawari-8 (H8) satellite was launched on 7 October 2014 by the Japan Meteorological Agency
92 (JMA). It started operation on 7 July 2015. The Advanced Himawari Imager (AHI) on board H8 can
93 provide multi-spectral observations with a high spatial resolution and high temporal frequency. It has 16
94 channels with a spatial resolution of 0.5-2 km. The AHI level 2 calibrated data provided by JMA have a
95 spatial coverage of 120° by 120° centred at 0° N, 140° E, and the observation area includes most of
96 eastern Asia, Australia and the Pacific Ocean. In addition, the AHI provides full-disk observations every
97 10 minutes. AHI level 2 calibrated data provided by the JMA and downloaded from the Japan Aerospace
98 Exploration Agency (JAXA) Earth Observation Research Center (EORC) were used
99 (<http://www.eorc.jaxa.jp/ptree/terms.html>).

100 **2.3 OMI/Aura**

101 The OMI sensor aboard the Aura satellite measures the Earth in the ultraviolet (UV) and visible spectra
102 (270-550 nm) with a wide swath. The OMI provides a parameter called the UV aerosol index (UV-AI),
103 which is a qualitative parameter that detects UV-absorbing aerosols. The UV-AI is sensitive to absorbing
104 aerosols, including mineral dust, black carbon, and biomass burning aerosols (Eck et al., 2001). Therefore,
105 the UV-AI can be used to identify aerosol types through positive values for dust and biomass burning
106 particles and near-zero or small positive values for clouds and weakly absorbing aerosols (Torres et al.,
107 2007). In addition, the UV-AI can be obtained under both cloudy and cloudless conditions. The surface

108 reflectance also has no impact on the UV-AI, which makes it capable of detecting absorption by aerosols
109 over highly reflective surfaces (Torres et al., 2007). Since this dust event occurred in May, a high UV-AI
110 can be a good indicator of high dust aerosol loading when combined with CALIPSO observations, as
111 Aura and CALIPSO have similar equatorial crossing times. Here, level 3 OMI UV-AI data were used
112 with a $0.125^\circ \times 0.125^\circ$ spatial resolution.

113 **2.4 CALIOP/CALIPSO**

114 The Cloud-Aerosol Lidar with Orthogonal Polarization (CALIOP) instrument on board the CALIPSO
115 satellite provides vertical profiles of the elastic backscatter at two wavelengths (532 nm and 1064 nm)
116 during both day and night. The CALIOP payload also provides linear depolarization at 532 nm that can
117 be used to identify dust aerosols since dust aerosols have a high linear depolarization ratio due to their
118 non-sphericity. Aerosol types are also provided in the CALIPSO aerosol product. The CALIPSO
119 algorithm defines six aerosol types, including smoke, dust, polluted dust, clean continental, polluted
120 continental, and marine (Omar et al., 2009; Omar et al., 2013). It has been evaluated that the CALIPSO
121 aerosol classification works well in most cases (Wu et al., 2014). It should be noted that the accuracy of
122 aerosol detection is decreased over highly reflected land surfaces such as deserts and snow-covered
123 regions. Here, CALIPSO level 2 vertical feature mask (VFM) aerosol layer products were used to provide
124 independent information about dust aerosols, especially for the night-time, as the signal-to-noise ratio
125 during the night-time is better than that during the daytime for CALIPSO (Liu et al., 2009). The VFM
126 products have a vertical resolution of 30 m below 8.2 km, 60 m for 8.2-20.2 km, and 180 m for 20.2-
127 30.1 km (Winker et al., 2007). The dust vertical distribution and dust layer height, were analysed using
128 CALIPSO VFM data.

129 **2.5 AERONET data**

130 The AERONET is a ground-based remote sensing aerosol network (Holben et al., 1998) that provides
131 spectral aerosol optical depth (AOD) and inversion products derived from direct and diffuse radiation
132 measurements by Cimel sun/sky-radiometers (Dubovik et al., 2006). The inversion products include both,
133 microphysical parameters (e.g., the size distribution and complex refractive index) and radiative
134 properties (e.g., the single-scattering albedo and phase function) (Dubovik et al., 2006).

135 In this study, Level 1.5 cloud screened data including both sun direct data (Version 2 and Version 3) and

136 Inversion data (Version 2) from four AERONET sites in the study area were used to analyse the temporal
 137 variations in aerosol properties, including the AOD, the extinction Ångström exponent (EAE), volume
 138 size distribution (VSD), and single-scattering albedo (SSA). Fig. 1 shows the locations of the four sites
 139 (white circles), namely, AOE_Baotou, Beijing, Xuzhou-CUMT, and Ussuriysk.

140 2.6 PM measurements

141 There are thousands of air quality stations over China that can provide hourly PM measurements during
 142 both, day-time and night-time. In addition, the measurements are free from the influences of clouds,
 143 making it a perfect complement to AERONET observations and satellite observations. Ground-based
 144 measurements of the PM mass concentration over the Chinese mainland were collected to evaluate the
 145 dust-affected areas and to further analyse the transport of the dust plume. Furthermore, the temporal
 146 variations in the PM concentrations at 14 typical stations were analysed in detail to examine the
 147 propagation of dust particles in different directions. Detailed information about these 14 air quality
 148 stations is given in Table 1.

149 **Table 1. The cities and locations of the 14 air quality stations to examine the propagation of dust particles**

City (Site)	Longitude (°)	Latitude (°)	City (Site)	Longitude (°)	Latitude (°)
Bayannao'er (BYN)	107.5936	40.916	Shanghai (SHS)	121.536	31.2659
Changsha (CSS)	112.9958	28.3586	Taiyuan (TYS)	112.5583	37.7394
Chengde (CDS)	117.9664	40.9161	Tianshui (TSS)	105.7281	34.5814
Guangyuan (GYS)	105.8153	32.4246	Tongliao (TLS)	122.2603	43.6267
Heihe (HHS)	127.4961	50.2486	Weihai (WHS)	122.0508	37.5325
Huhhot (HHT)	111.7277	40.8062	Zhengzhou (ZZS)	113.6113	34.9162
Jiangchang (JCS)	102.1878	38.5247	Zhongwei (ZWS)	105.18	37.0172

150 2.7 HYSPLIT trajectories and meteorological data

151 The HYSPLIT model developed by NOAA's Air Resources Laboratory was employed (Draxler and
 152 Rolph, 2013). It is widely used for computing air mass forward/backward trajectories to analyse the
 153 transport of air/pollution parcels. The start/end point as well as the time of the HYSPLIT computation
 154 can be customized. Here, HYSPLIT was used to generate air mass backward trajectories to trace the air

155 movement. The data from Global Data Assimilation System (GDAS) with a spatial resolution of 0.5
156 degree were used as meteorology input. The backward trajectories ending at 9 selected points were
157 calculated for determining the dust source.

158 The meteorological data including wind vectors and geopotential height (GH) from ECMWF ERA
159 Interim reanalysis dataset were also used ([http://apps.ecmwf.int/datasets/data/interim-full-](http://apps.ecmwf.int/datasets/data/interim-full-daily/levtype=pl/)
160 [daily/levtype=pl/](http://apps.ecmwf.int/datasets/data/interim-full-daily/levtype=pl/)). The distribution of the wind direction, wind speed and GH with a spatial resolution
161 of 1 degree during 3-8 May 2017 were analysed to understand the origin and transport of the dust storm.

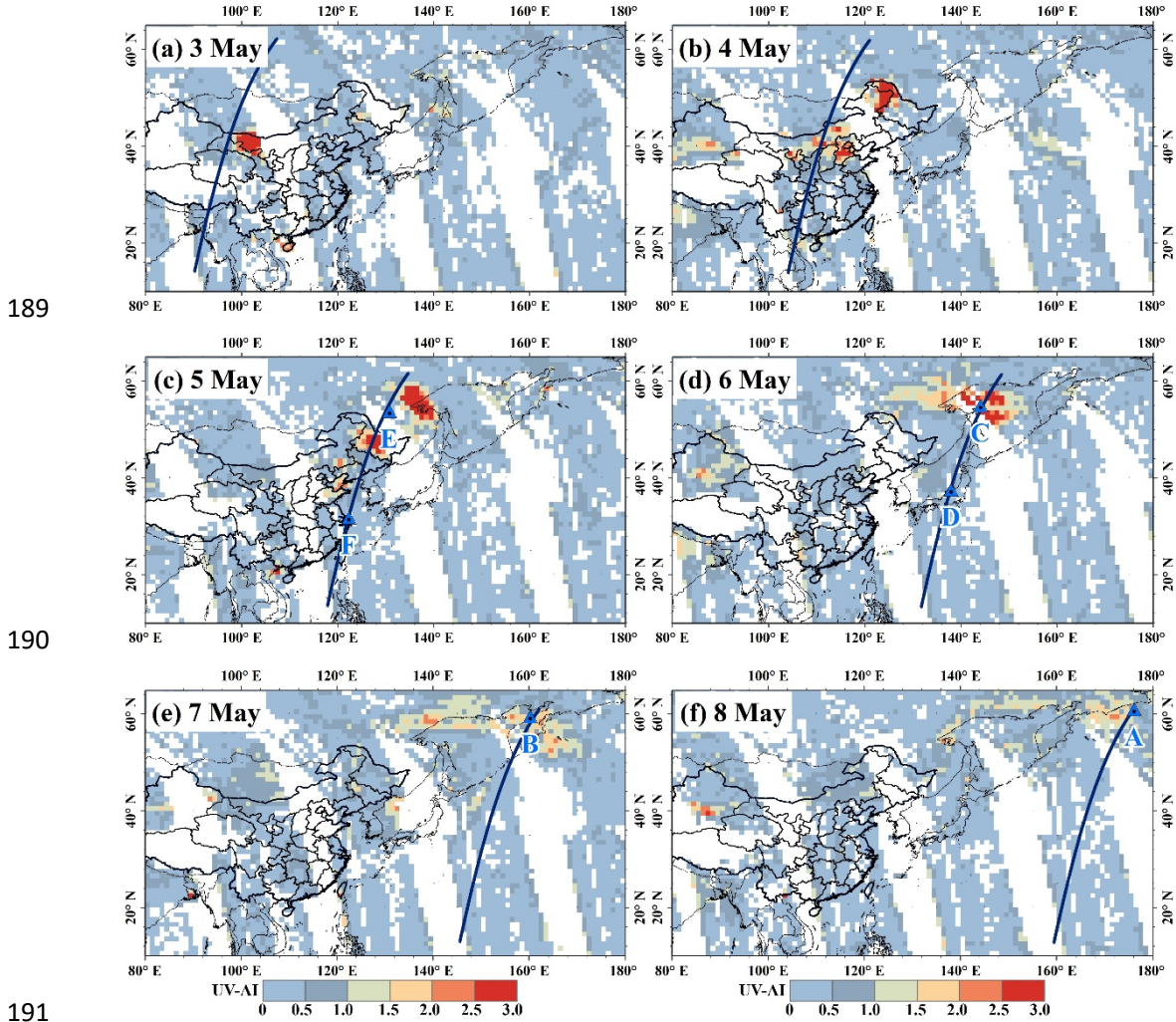
163 3. Results

164 3.1 Source and transport of the dust event

165 Fig. 2 shows the spatial distribution of the UV-AI over East Asia from 3 to 8 May 2017 obtained from
166 the OMI-Aura observations. High AI values (>2.0) can be observed over northern China, especially over
167 Inner Mongolia on 3 May, north eastern China on 4-5 May, and south eastern Russia on 5-6 May. The
168 OMI-AI time series revealed one of the long-distance transport path of the strong absorbing aerosols that
169 originated from the Gobi Desert, i.e., moving towards the east and then northeast (hereafter referred to
170 as northeast direction for simplicity). This can be explained by the strong west and southwest wind
171 evident in Fig. 3, which showing the spatial distribution of the wind vectors and geopotential height field
172 at 500-pha level at 06:00 UTC during 3-8 May. The dust storm was initially developed over western
173 Inner Mongolia ($\sim 40^\circ$ N, 100° E) on 3 May 2017 (see Fig. 2a) and then swept through the North China
174 plain and reached north eastern China ($\sim 50^\circ$ N, 125° E) on 4 May 2017 due to a strong west wind (Fig.
175 2b and Fig. 3). On 5 May, the dust plume was transported to the western Sea of Okhotsk ($\sim 56^\circ$ N, 140° E).
176 For the next two days, the elevated dust plume travelled across the Sea of Okhotsk and finally reached
177 the Bering Sea (see Fig. 2e-f). Furthermore, there is a small portion of the high AI values in the Japan
178 Sea on 7 May (Fig. 2e) indicating that there is a second dust transport path of all the way east and the
179 Korean Peninsula and Japan were affected. This is because the wind field diverged to two directions at
180 North China plain, i.e., towards northeast and towards east (Fig. 3).

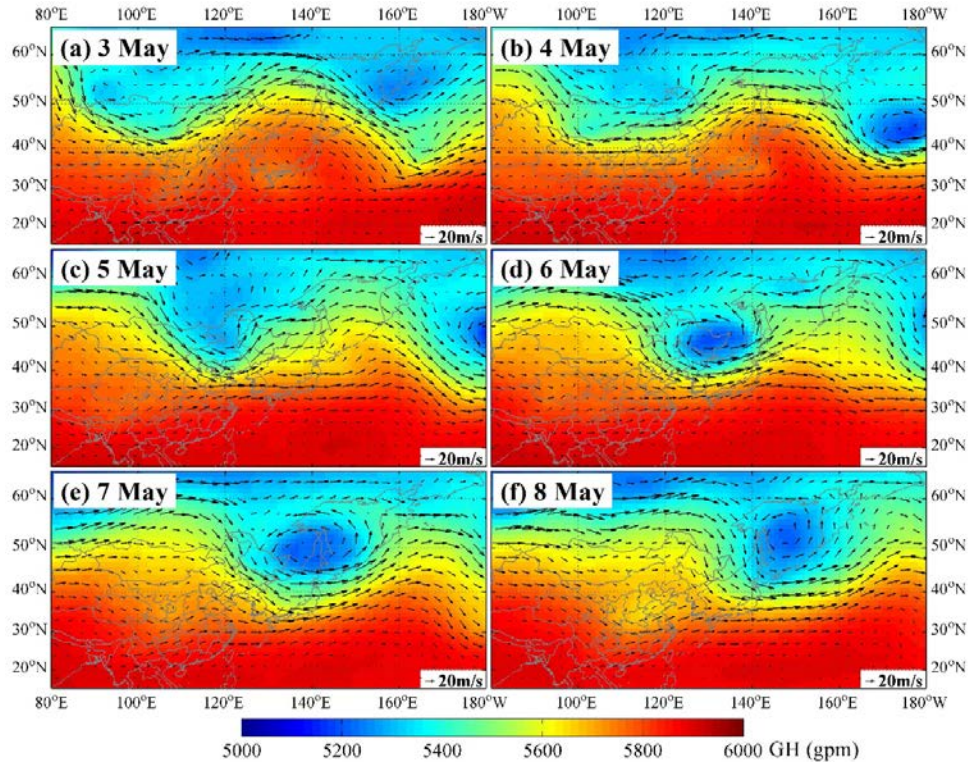
181 To confirm that the high AI values were caused by dust aerosols, CALIPSO observations that passed
182 through the high AI value regions during the night-time were employed to provide aerosol type and
183 vertical distribution information. Fig. 4 depicts the vertical distributions of the aerosol types for six

184 overpass trajectories shown in Fig.2 (the deep blue lines). The dust aerosol (yellow) in Fig. 4
 185 corresponded well to the high AI value region in Fig. 2. Furthermore, the dust layer was thick and
 186 distributed from the surface to a 10 km height. Moreover, part of the aerosol layer was marked as the
 187 polluted dust subtype over the Central China on 4 May and over the northern China on 5 May. This may
 188 be explained by the mixture of dust and anthropogenic pollution.



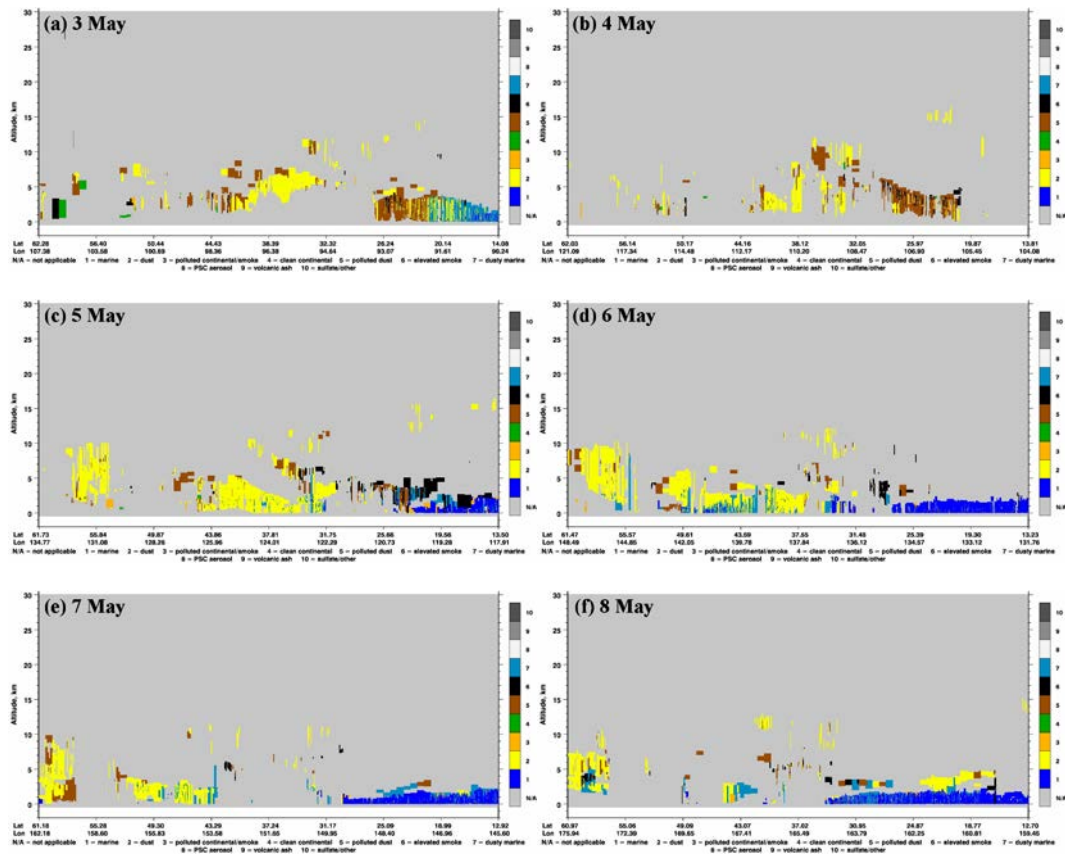
191
 192 **Fig. 2. a-f. Spatial distributions of the OMI UV AI from 3 to 8 May 2017. The deep blue lines are the overpass**
 193 **trajectories of the used CALIPSO observations on that day. The blue triangles are the end points of the**
 194 **HYSPLIT computation.**

195
 196 Fig. 5 shows the backward trajectories at different sources (the blue triangles in Fig. 2) during 5-8 May
 197 2017. The trajectories are computed at three different altitudes (1000 m, 2000 m, and 3000 m). The
 198 HYSPLIT backward trajectory analysis revealed that the air masses that reached the Bering Sea (Fig. 5a),
 199 the Kamchatka Peninsula (Fig. 5b), the Sea of Okhotsk (Fig. 5c), and the Japan Sea (Fig. 5d) originated
 200 from the Gobi Desert. This result is consistent with that from the OMI-AI and CALIPSO aerosol type
 201 information.



202

203 Fig. 3. a-f. Spatial distribution of wind vectors and geopotential height (GH) at 500-hPa level at 06:00 UTC
 204 during 3-8 May. The GH and wind vectors were derived from ECMWF ERA Interim reanalysis dataset.



205

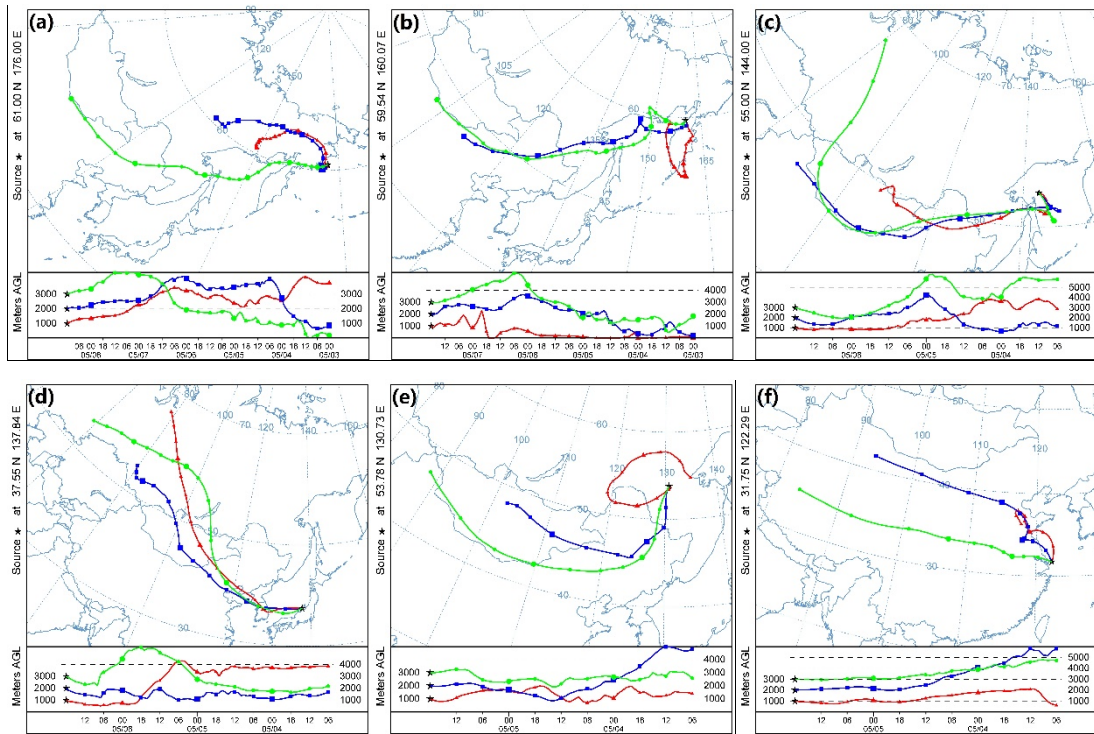
206

207

208 Fig. 4. a-f. CALIPSO aerosol subtypes on 3-8 May 2017, corresponding to the overpass trajectories shown in
 209 Fig. 2. The dust aerosol is shown in yellow.

210

211

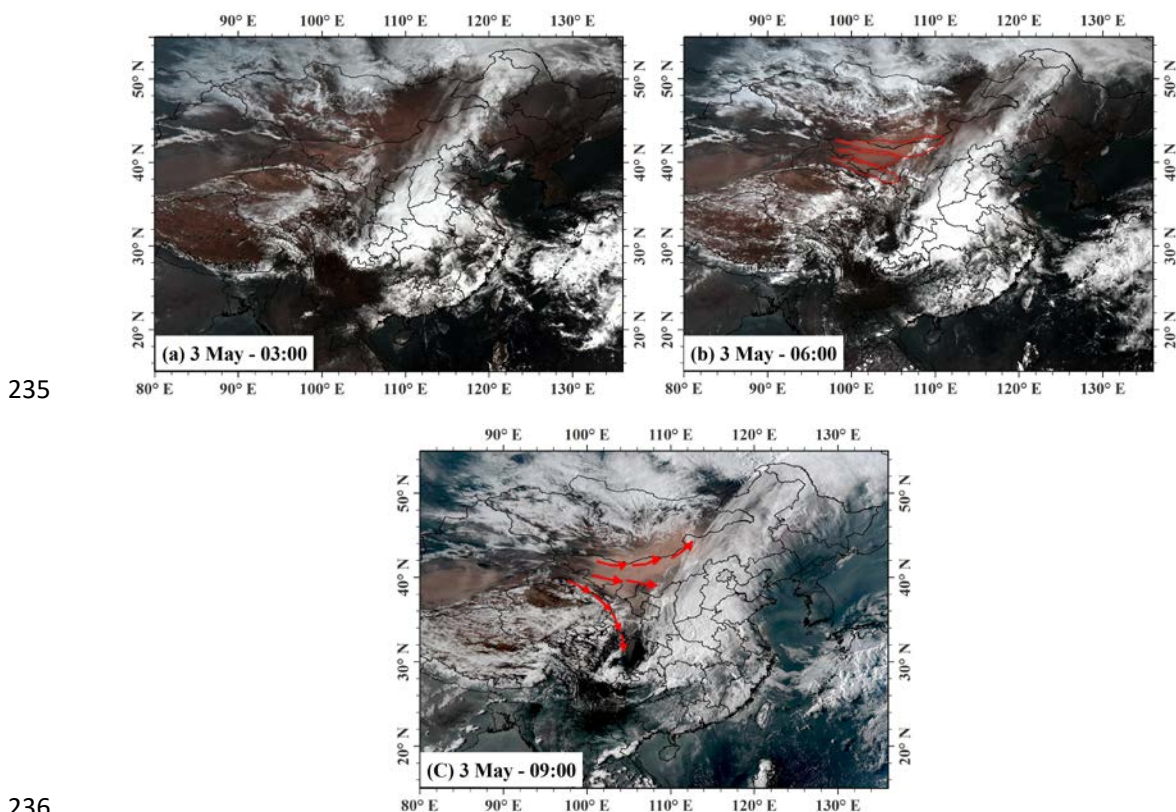


212

213 **Fig. 5. Backward trajectories derived from the HYSPLIT model at different locations during 5-8 May 2017:**
214 **(a) 132-h back trajectories ending at the Bering Sea on 8 May, (b) 108-h back trajectories ending at the**
215 **Kamchatka Peninsula on 7 May, (c-d) 84-h back trajectories ending at the Sea of Okhotsk and the Sea of**
216 **Japan on 6 May, respectively, and (e-f) 60-h back trajectories ending at southeastern Russia and the Yangtze**
217 **River estuary region on 5 May, respectively.**

218 For a better view of the dust plume transport, the high-temporal-resolution observations from the
219 Himawari-8/AHI true-colour composite images on 3 May (Fig. 6) and 4 May (Fig. 7) were shown. The
220 results in Fig. 6 suggest that the strong dust storm was originated from the western part of the Gobi Desert
221 and was formed by several distinct dust clusters (Fig. 6b). In the morning of 3 May, only a small area
222 was covered by a dust plume in the Gobi Desert (Fig. 6a), as the dust storm continuously increased and
223 quickly moved. Part of the dust plume over south western Inner Mongolia moved along the edge of the
224 Qinghai-Tibet Plateau and then finally reached the northern Sichuan basin (Fig. 6c), revealing the third
225 path of the dust transport. This path of the dust transport is not revealed in the OMI AI time series maps
226 possibly because the dust in this path is not very severe. On the other hand, thick dust plume travelled
227 along the China-Mongolia border with continually increasing dust intensity and moved quickly towards
228 the northeast and east. In addition, in the late afternoon of 4 May 2017 (Fig. 7), another thick dust plume
229 was found that originated from northern Inner Mongolia (Fig. 7c) that was quickly transported eastward
230 due to strong westerly winds. High-frequency observations from the AHI presented more information

231 about this severe dust storm, revealing multi-plumes propagation and several different transport
232 directions, including south eastward, eastward and north eastward. The longest-distance transport
233 occurred in the north eastward direction, as OMI-AI and CALIPSO-VFM illustrated in the previous
234 section, and finally arrived at the Bering Sea.



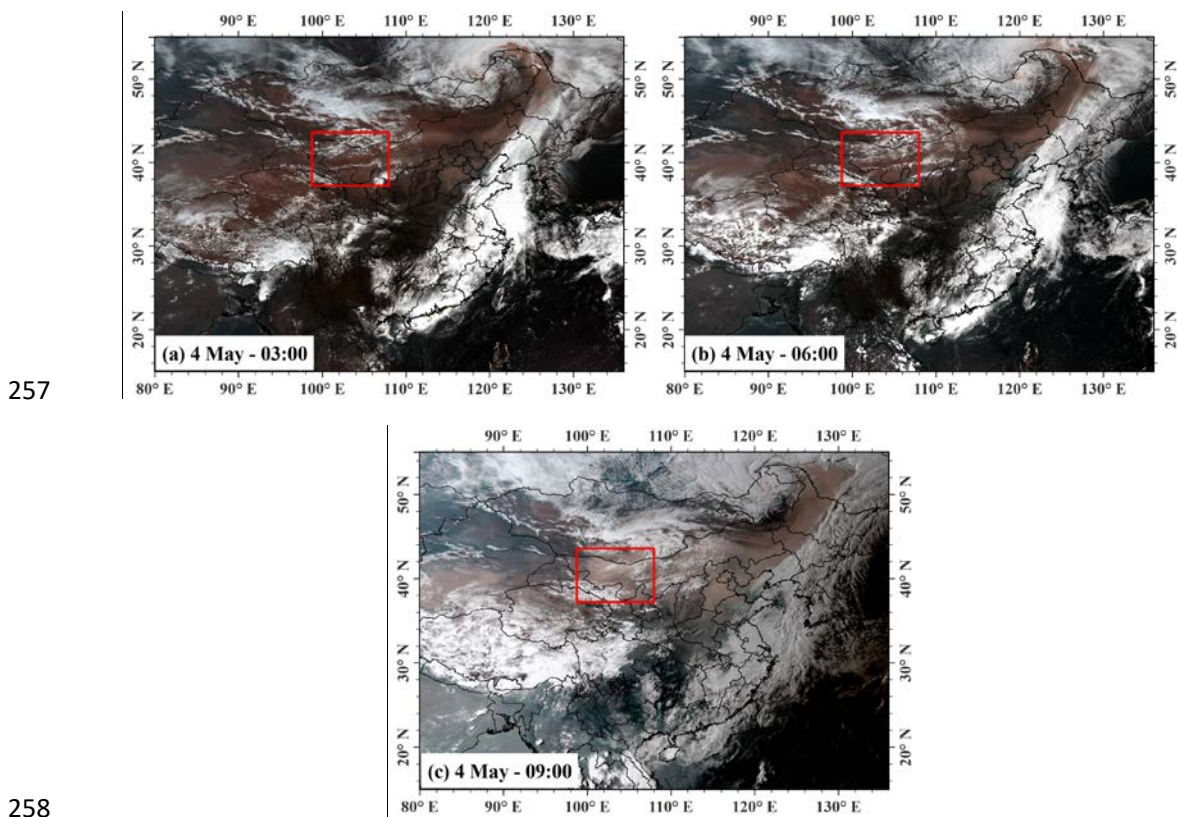
237 **Fig. 6. True-colour composite images of mainland China (a-c) from AH1 data over a 3-h interval on 3 May**
238 **2017. (a) 03:00, (b) 06:00, (c) 09:00. The red polygons in (b) are dust clusters. The arrows in (c) represents**
239 **the dust transport directions.**

240

241 3.2 PM characterization in China during the dust event

242 In this section, the temporal variations in the $PM_{2.5}$ ($PM < 2.5 \mu m$ in aerodynamic diameter) and PM_{10}
243 mass concentrations over mainland China were analysed and the third path of the dust transport, i.e.,
244 towards southeast, is obvious. Fig. 8 depicts the hourly PM_{10} concentration distribution over mainland
245 China over a 12-h interval from 06:00 a.m. on 5 May to 06:00 p.m. on 7 May (Beijing time) using a total
246 of 1350 stations, the PM values are real-time measurements per hour. The PM concentration value less
247 than 200 were shown in grey. Interestingly, south eastward transport was revealed through the intensive
248 PM concentration measurements, which was almost missed by most of the satellite observations because

249 the central and eastern China were covered by cloud during 5-7 May. The high PM₁₀ concentration was
250 mostly distributed over 35-40°N at 06:00 on 5 May (Fig. 8a). After 12 hours, the dust plume moved to
251 Shandong Peninsula (eastern China close to the Yellow Sea) and further affected Central China on 6 May
252 (Figs. 8 c-d). On May 7 the dust events were found in most stations of eastern and central China (Figs. 8
253 e-f). The southward propagation of the dust plume caused a high PM₁₀ concentration (>500) in south-
254 central China (~28° N, 118° E) as well as the eastern coastal areas including the Shandong Peninsula
255 (eastern China close to the Yellow Sea), and the Yangtze River Delta.
256



259 **Fig. 7. True-colour composite images of mainland China (a-c) from AHI data over a 3-h interval from 03:00**
260 **UTC to 09:00 UTC on 4 May 2017. (a) 03:00, (b) 06:00, (c) 09:00. The red rectangles marked the area where**
261 **another dust plumes originated from in the afternoon of 4 May.**

262

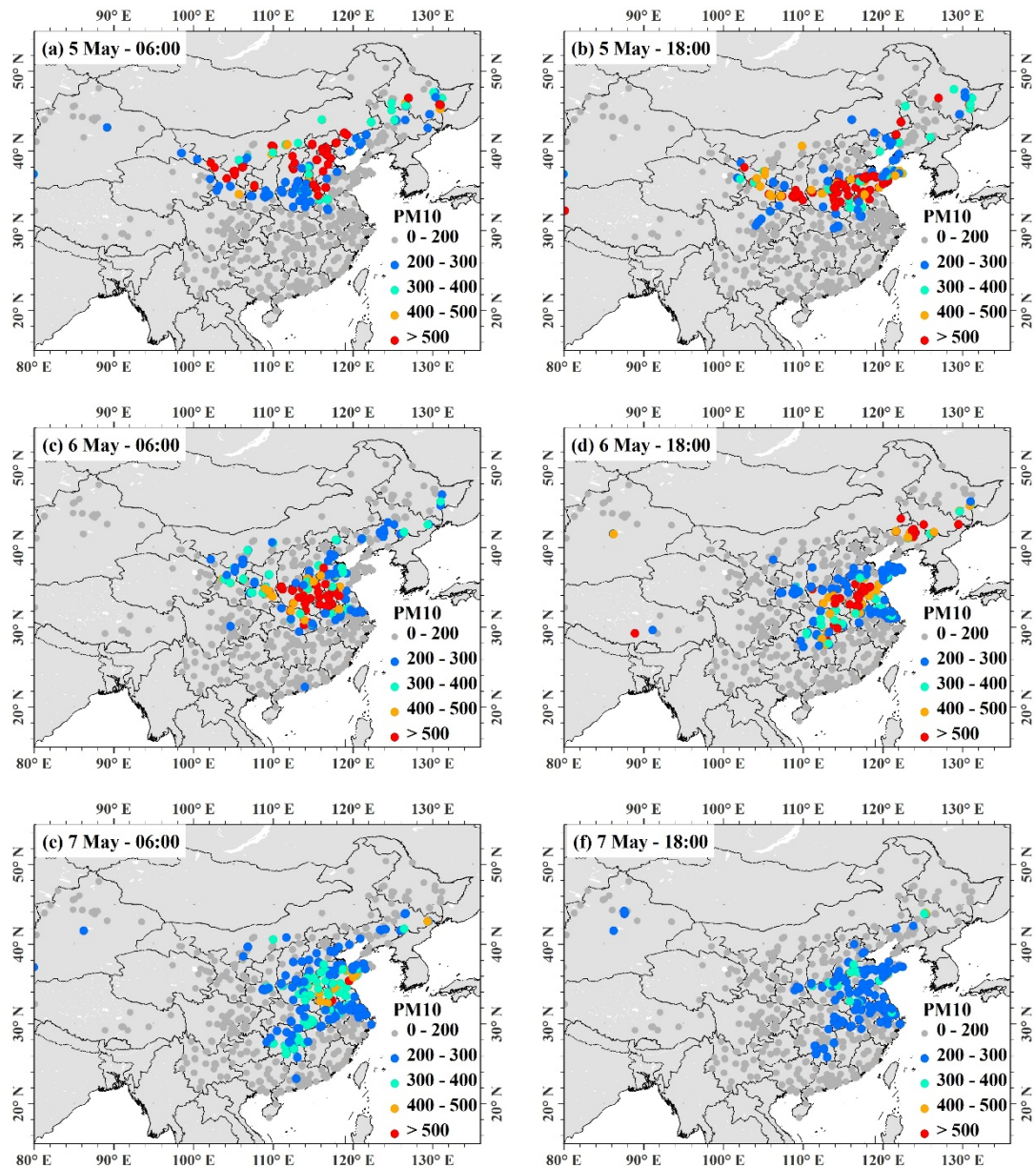
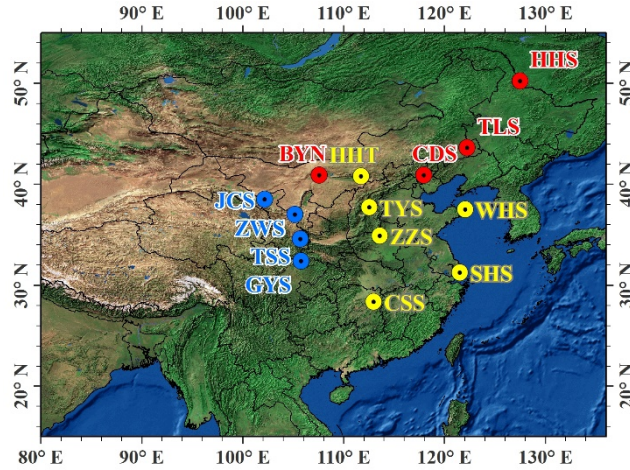


Fig. 8. PM₁₀ mass concentrations measured by ground-based air quality stations in mainland China over a 12-h interval from 06:00 on May 5 to 18:00 on May 7.

To obtain better insight into the dust evolution, measurements from 14 typical air quality stations (the colour circles in Fig. 9) situated within the source and transport areas of the dust were analysed in detail. As the PM concentration was measured during both the day-time and night-time, the data can provide much more information about this continuous dust plume. Fig. 10 shows the PM temporal variations along three different dust transport directions during 2 to 7 May, including the northeastward propagation (a), southward propagation (b) and southeastward propagation (c). It is clearly observed that both the PM_{2.5} and the PM₁₀ increased dramatically, and the PM₁₀ showed much larger increments than the PM_{2.5} during this dust event from all three figures.



278

279 **Fig. 9. The locations of the 14 air quality stations. Different color represent different dust transport directions**
 280 **names by sequencing site names in the time order when the dust passes: the northeast direction of BYN-CDS-**
 281 **TLS-HHS, and the two south directions of JCS-ZWS-TSS-GYS and HHT-TYS-ZZS-CSS. Note the east**
 282 **direction travelling to the Japan Sea is not shown as most of its path is over sea without air quality stations.**

283

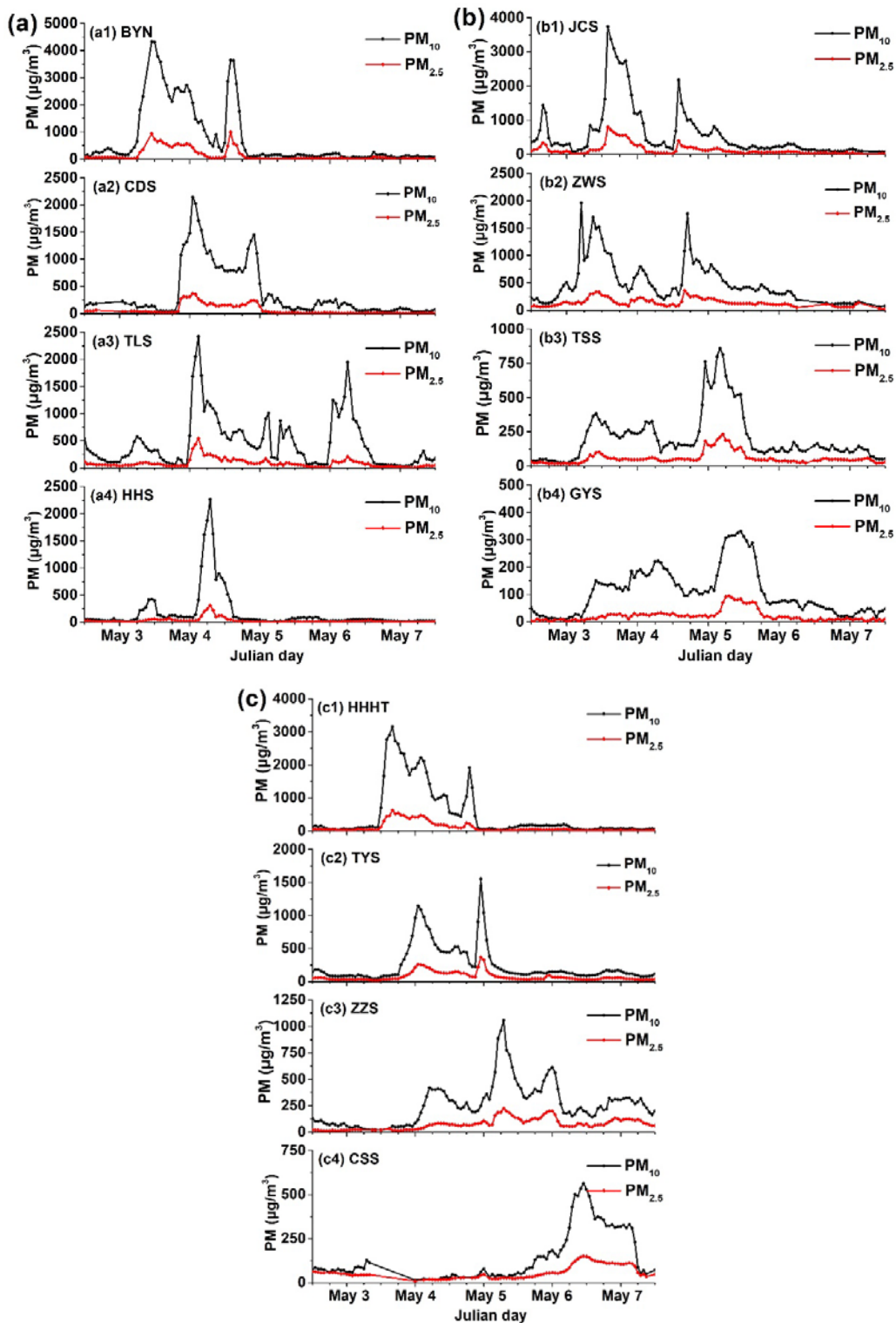
284 As Fig. 10a illustrates, the sharp increase in the PM mass concentration was first observed at BYN station
 285 on the morning of 3 May, followed by the CDS (23:00 UTC on 3 May) and TLS (8:00 UTC on 4 May),
 286 and reached the northeastern-most city, namely, Heihe (HHS) (06:00 UTC on 4 May). The maximum
 287 value of PM₁₀ concentration at BYN reached 4333 μg/m³ on 4 May. High PM₁₀ concentrations occurred
 288 successively at those sites. These drastic changes in the PM₁₀ are in agreement with the dust movements
 289 revealed from the satellite observations.

290 PM measurements at 4 stations distributed along the eastern edge of the Qinghai-Tibet Plateau, including
 291 JCS, ZWS, TSS and GYS, are shown in Fig. 10b. Within one day, the dust plume was transported across
 292 Gansu and reached GYS, which is located in the Sichuan Basin. This transport was also revealed by the
 293 high-frequency AHI observations (Fig. 6c), although it is not as noticeable.

294 Fig. 10c displays the PM concentration variations over the cities located in Central China, including
 295 Taiyuan (TYS), Zhengzhou (ZZS), and Changsha (CSS). In addition, high PM concentrations were
 296 observed in the coastal areas of eastern China, as shown in Fig. 11. Note that the increases of PM₁₀ are
 297 much larger than the increments of PM_{2.5} in these stations, suggesting that the dust particles were
 298 transported to southern and eastern China.

299 To confirm this southward propagation of dust, the backward trajectories ending at GYS, CSS, and SHS
 300 were analysed by HYSPLIT, as shown in Fig. 12. The trajectories are computed at three different altitudes

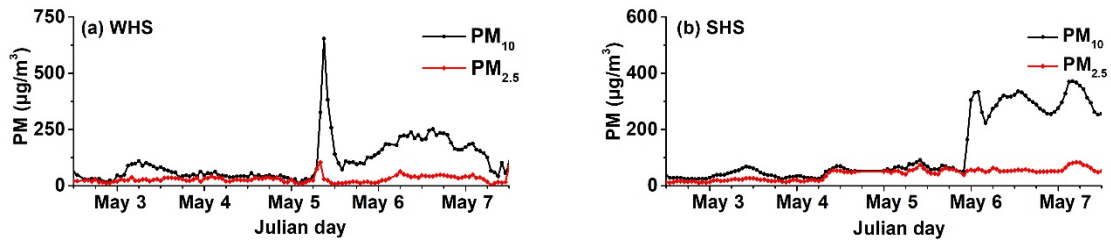
301 (500 m, 1000 m, and 1500 m). The northwestern air masses at all three locations originated from sources
 302 in the Gobi Desert. Thus, dust could be the main reason for the sudden increase in the PM concentrations.



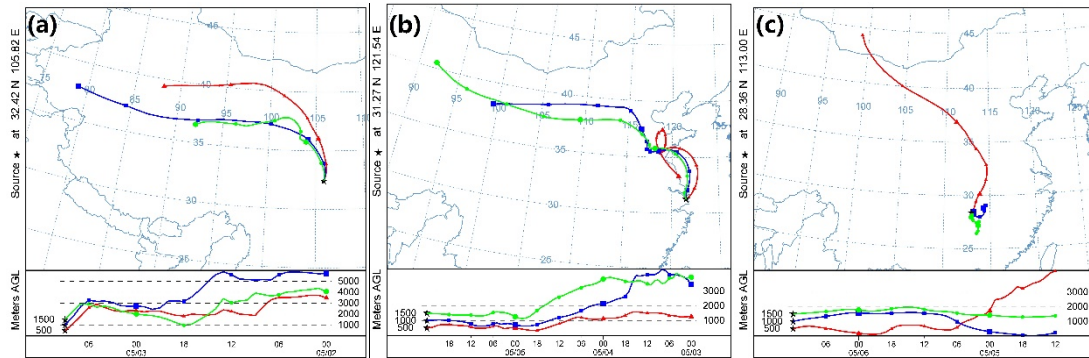
303

304

305 **Fig. 10.** Time series of the PM_{2.5} (red curves) and PM₁₀ concentrations (black curves) during 2-7 May at 14
 306 air quality stations in three directions: (a) northeastward propagation, including (a1) BYN, (a2) CDS, (a3)
 307 TLS and (a4) HHS, (b) southward propagation, including (b1) JCS, (b2) BYS, (b3) TSS and (b4) GYS, and
 308 (c) southeastward propagation, including (c1) HHT, (c2) TYS, (c3) ZZS and (c4) CSS.



309
 310 **Fig. 11. Time series of the PM_{2.5} (red curves) and PM₁₀ concentrations (black curves) during 2-7 May at (a)**
 311 **WHS and (b) SHS.**



312
 313 **Fig. 12. Backward trajectories derived from the HYSPLIT model at different altitude levels (500 m, 1000 m,**
 314 **and 1500 m) at (a) GYS on 3 May, (b) SHS on 6 May, and (c) CSS on 6 May 2017.**

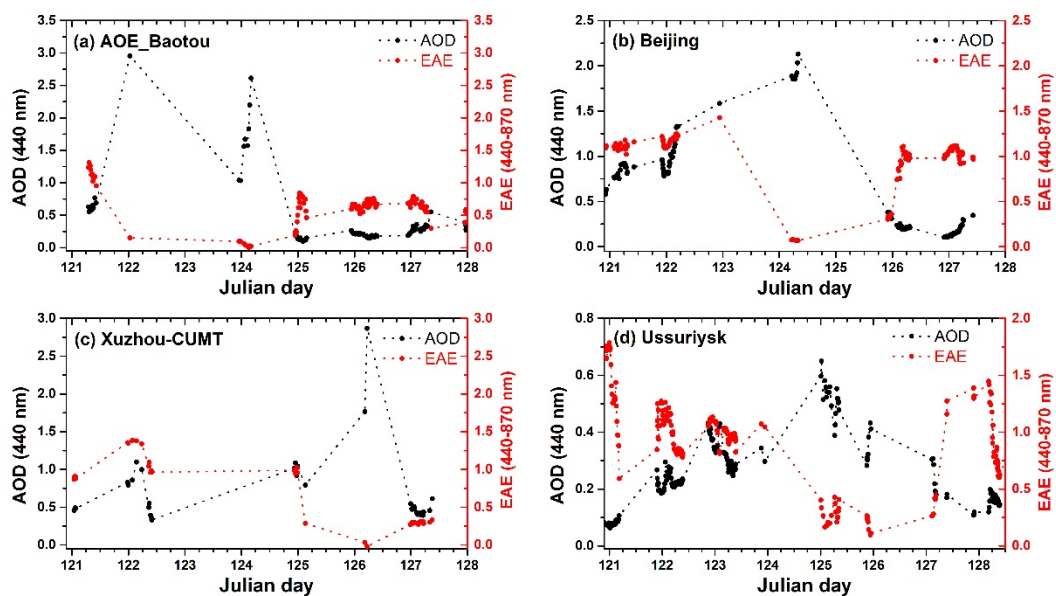
315 **3.3 Aerosol property variations during the dust event**

316 In order to understand the effects of dust storm on aerosol properties, the changes in the aerosol properties
 317 at four typical AERONET stations located in the study area were investigated. The longitudes of
 318 AOE_Baotou, Beijing, and Ussuriysk increase from west to east, and the latitudes of AOE_Baotou,
 319 Beijing, and Xuzhou-CUMT decrease from north to south (Fig. 1). Several key aerosol properties,
 320 including the AOD, EAE, SSA, and aerosol VSD, were analysed in detail.

321 The temporal variations in the daily AOD and EAE at the four AERONET sites during dusty and non-
 322 dusty days are plotted in Fig. 13. The maximum AODs at 440 nm caused by the dust storm were 2.96,
 323 2.13, 2.87, and 0.65 at AOE_Baotou, Beijing, Xuzhou-CUMT, and Ussuriysk, respectively. The
 324 maximum AOD at Baotou (the westernmost station) was recorded on 2 May 2017 and became lower
 325 afterwards. Then, the dust storm moved eastward, and the highest AOD value of 2.13 was observed over
 326 Beijing on 4 May 2017. As the dust storm travelled northeastward, the Ussuriysk, located in southern
 327 Russia, was affected with a slight increase in the AOD (from ~0.25 to ~0.65) and a sharp decrease in the
 328 EAE (from ~1 to ~0.1) on 5 May 2017. Xuzhou-CUMT, which is located in southern Central China, was
 329 also severely affected by the strong dust on 4-5 May. The maximum AODs occurred at different times at

330 the four sites due to the movement of the dust storm. In addition, there are obvious negative correlations
 331 between the AOD and EAE during the dust event. The dust storm brought numerous large particles,
 332 causing the low EAE and high extinction properties.

333 The SSA is strongly related to absorption/scattering characteristics. Fig. 14 shows the variability of the
 334 spectral SSA before, during and after this dust event, and the monthly average as a benchmark. The SSA
 335 at longer wavelengths (e.g., 675, 870, and 1020 nm) at AOE_Baotou varied from ~0.8 to ~0.9 during
 336 non-dusty days (1 May and 2 May), and the monthly average of SSA_{675nm} (SSA at 675 nm) was
 337 approximately 0.9. In contrast the SSA_{675nm} increased to 0.97-0.98 during dust days (2 and 4 May). In
 338 addition, the spectral behaviour of the SSA showed significant differences. The SSA increased with the
 339 wavelength on 2 May and 4 May. Especially on 4 May, the SSA largely increased from 440 nm to 675
 340 nm (from 0.93 to 0.98), and the dSSA ($dSSA=SSA_{870nm}-SSA_{440nm}$) also increased to 0.07. According to
 341 Dubovik et al. (2002), mineral dust aerosols tend toward a dSSA value greater than 0.05. In contrast, the
 342 monthly average of the spectral SSA as well as the spectral SSA during non-dusty days obviously
 343 decreased with the increase in wavelength. The high SSA and increasing spectral behaviour indicates
 344 that aerosol particles are dominated by large particles with strong scattering. However, it was noticed
 345 that the SSA_{440nm} on 2 May was high. This could be explained by the mixture of dust aerosols with large
 346 amounts of anthropogenic aerosols from industrial emissions, which are more absorbent.

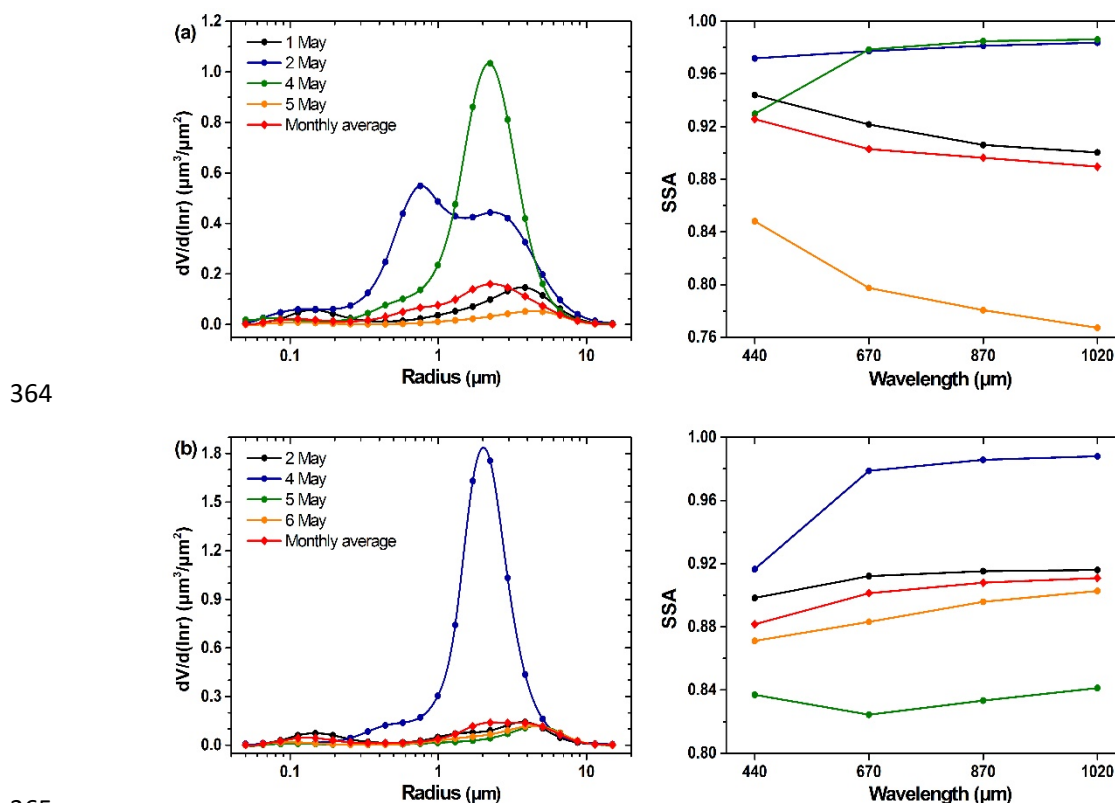


347
 348 **Fig. 13. Variations in the AOD (440 nm) and Ångström exponent (440-870 nm) at (a) AOE_Baotou, (b)**
 349 **Beijing, (c) Xuzhou-CUMT, and (d) Ussuriysk during 1-8 May 2017.**

350 Similar properties can be observed over Beijing, as the dusts over both Baotou and Beijing have similar

351 sources. However, there are still a few differences. The monthly average of the spectral SSA in Beijing
 352 was lower than that in AOE_Baotou, and an opposite spectral dependence was observed between these
 353 two sites. Baotou was affected by a greater quantity of industry emissions than Beijing, as it is a heavy
 354 industry city.

355 The VSD variation showed a more obvious distinction between dusty and non-dusty days. As Fig. 14
 356 illustrates, the particle volumes of fine-mode aerosols are comparable with those of coarse-mode aerosols
 357 in Beijing and Baotou during non-dusty days. The strong dust storm caused a dramatic increase in coarse-
 358 mode particles. The volume median radius also showed differences between dusty and non-dusty days.
 359 The VSD peaks occurred at radii of $\sim 2 \mu\text{m}$ with peak values of 1.05 and 1.8 on 4 May at Baotou and
 360 Beijing, respectively. Meanwhile, no significant variation was observed for fine-mode particles. It is
 361 observed that the volumes of both fine- and coarse-mode particles were large at AOE_Baotou on 2 May
 362 due to the combination of fine-mode aerosols with dust particles. This also explains the spectral SSA
 363 behaviour on that day.



366 **Fig. 14. Variations in the daily aerosol volume size distribution and spectral SSA during the dust event at (a)**
 367 **AOE_Baotou and (b) Beijing. Different colours represent different days, and the red curves represent the**
 368 **average VSD and SSA in May 2017. There was no VSD and SSA inversion product for Xuzhou-CUMT and**
 369 **Ussuriysk sites during May 3-8 2017.**

370 **4. Conclusions**

371 In this study, we described a strong dust storm that occurred in northern China and Mongolia in early
372 May 2017. The source and transport were investigated using multi-satellite data (including OMI,
373 CALIPSO, and AHI), ground-based measurements (including PM measurements and AERONET
374 observations), and HYSPLIT model computations. Benefiting from the high frequency of geostationary
375 satellite observations, the rapid spatial-temporal variations in the dust plume were captured, including
376 the continuous dust storms originating from the Gobi Desert region and different transport directions
377 over China region. The OMI-AI and CALIPSO observations during the night-time provided more
378 comprehensive information with larger coverage for the large-scale transport and vertical distribution of
379 the dust plume. Intensive measurements (in both time and space) of the PM mass concentration revealed
380 additional details when the region was covered by thick clouds and CALIPSO covered limited
381 observation areas. The backward trajectories computed from the HYSPLIT model also confirmed the
382 dust transport directions. From the combined observations, this severe dust storm was found to originate
383 from the Gobi Desert, and travel to three different directions affecting large areas of China, including
384 northern China, southeast China, and even Central China due to the strong winds. In addition, southern
385 and eastern Russia and the Bering Sea were influenced by the long-distance transport of the strong dust
386 plume. The aerosol properties (EAE, SSA, and VSD) have changed greatly during the dusty days as
387 numerous large particles contributed to strong scattering and extinction. Overall, the combined
388 observations of satellite and ground-based data contributed to the comprehensive monitoring of the
389 source and long-distance transport of the dust storms, providing complete information on the spatial-
390 temporal distribution.

391 **Acknowledgements**

392 This work was supported in part by the Major Innovation Projects for Building First-class Universities
393 in China's Western Region under Grant No. ZKZD2017004. We gratefully acknowledge the support by
394 the National Natural Science Foundation of China (Grant No. 41471306) and the Strategic Priority
395 Research Program of the Chinese Academy of Sciences (Grant No. XDA19070202). The OMI and
396 CALIOP data were obtained from NASA. The AHI data were supplied by the P-Tree System, Japan
397 Aerospace Exploration Agency (JAXA) (<http://www.eorc.jaxa.jp/ptree/terms.html>). The PM data used

398 in this work were acquired from the China Meteorological Administration. Many thanks are due to the
399 principal investigators of the AERONET sites used in this paper for maintaining their sites and making
400 their data publicly available. We would also like to thank the anonymous reviewers for their valuable
401 comments, which greatly improved the quality of this manuscript.

402 **References**

403 Alam, K., Trautmann, T., Blaschke, T., and Subhan, F.: Changes in aerosol optical properties due to dust
404 storms in the Middle East and Southwest Asia, *Remote Sensing of Environment*, 143, 216-227,
405 10.1016/j.rse.2013.12.021, 2014.

406 Athanasopoulou, E., Protonotariou, A., Papangelis, G., Tombrou, M., Mihalopoulos, N., and
407 Gerasopoulos, E.: Long-range transport of Saharan dust and chemical transformations over the Eastern
408 Mediterranean, *Atmospheric Environment*, 140, 592-604, 10.1016/j.atmosenv.2016.06.041, 2016.

409 Badarinath, K. V. S., Kharol, S. K., Kaskaoutis, D. G., Sharma, A. R., Ramaswamy, V., and Kambezidis,
410 H. D.: Long-range transport of dust aerosols over the Arabian Sea and Indian region — A case study
411 using satellite data and ground-based measurements, *Global and Planetary Change*, 72, 164-181,
412 10.1016/j.gloplacha.2010.02.003, 2010.

413 Bangert, M., Nenes, A., Vogel, B., Vogel, H., Barahona, D., Karydis, V. A., Kumar, P., Kottmeier, C., and
414 Blahak, U.: Saharan dust event impacts on cloud formation and radiation over Western Europe,
415 *Atmospheric Chemistry and Physics*, 12, 4045-4063, 10.5194/acp-12-4045-2012, 2012.

416 Basha, G., Phanikumar, D. V., Kumar, K. N., Ouarda, T. B. M. J., and Marpu, P. R.: Investigation of
417 aerosol optical, physical, and radiative characteristics of a severe dust storm observed over UAE, *Remote
418 Sensing of Environment*, 169, 404-417, 10.1016/j.rse.2015.08.033, 2015.

419 Chen, Y., Luo, B., and Xie, S.-d.: Characteristics of the long-range transport dust events in Chengdu,
420 Southwest China, *Atmospheric Environment*, 122, 713-722, 10.1016/j.atmosenv.2015.10.045, 2015.

421 Creamean, J. M., and Prather, K. A.: Dust and Biological Aerosols from the Sahara and Asia Influence
422 Precipitation in the Western U.S, *Science*, 339, 1572-1578, 2013.

423 Dall'Osto, M., Harrison, R. M., Highwood, E. J., O'Dowd, C., Ceburnis, D., Querol, X., and Achterberg,
424 E. P.: Variation of the mixing state of Saharan dust particles with atmospheric transport, *Atmospheric
425 Environment*, 44, 3135-3146, 2010.

426 Dubovik, O., Sinyuk, A., Lapyonok, T., Holben, B. N., Mishchenko, M., Yang, P., Eck, T. F., Volten, H.,
427 Muñoz, O., Veihelmann, B., van der Zande, W. J., Leon, J.-F., Sorokin, M., and Slutsker, I.: Application
428 of spheroid models to account for aerosol particle nonsphericity in remote sensing of desert dust, *Journal*
429 *of Geophysical Research*, 111, 10.1029/2005jd006619, 2006.

430 Eck, T. F., Holben, B. N., Ward, D. E., Dubovik, O., Reid, J. S., Smirnov, A., Mukelabai, M. M., Hsu, N.
431 C., O'Neill, N. T., and Slutsker, I.: Characterization of the optical properties of biomass burning aerosols
432 in Zambia during the 1997 ZIBBEE field campaign, *Journal of Geophysical Research: Atmospheres*, 106,
433 3425-3448, 10.1029/2000jd900555, 2001.

434 Fairlie, T. D., Jacob, D. J., and Park, R. J.: The impact of transpacific transport of mineral dust in the
435 United States, *Atmospheric Environment*, 41, 1251-1266, 2007.

436 Ginoux, P., Prospero, J. M., Torres, O., and Chin, M.: Long-term simulation of global dust distribution
437 with the GOCART model: correlation with North Atlantic Oscillation, *Environmental Modelling &*
438 *Software*, 19, 113-128, 2004.

439 Goudie, A. S.: Dust storms: recent developments, *Journal of Environmental Management*, 90, 89-94,
440 2009.

441 Guo, J., Lou, M., Miao, Y., Wang, Y., Zeng, Z., Liu, H., He, J., Xu, H., Wang, F., Min, M., and Zhai, P.:
442 Trans-Pacific transport of dust aerosols from East Asia: Insights gained from multiple observations and
443 modeling, *Environmental pollution*, 230, 1030-1039, 10.1016/j.envpol.2017.07.062, 2017.

444 Holben, B. N., Eck, T. F., Slutsker, I., Tanre, D., Buis, J. P., Setzer, A., Vermote, E., Reagan, J. A.,
445 Kaufman, Y. J., Nakajima, T., Lavenu, F., Jankowiak, I., and Smirnov, A.: AERONET - A federated
446 instrument network and data archive for aerosol characterization, *Remote Sensing of Environment*, 66,
447 1-16, 10.1016/s0034-4257(98)00031-5, 1998.

448 Huang, J., Patrick, M., Chen, B., Huang, Z., Liu, Z., Zhao, Q., Yi, Y., and Kirk, A. J.: Long-range transport
449 and vertical structure of Asian dust from CALIPSO and surface measurements during PACDEX, *Journal*
450 *of Geophysical Research Atmospheres*, 113, -, 2008.

451 Lee, Y. C., Yang, X., and Wenig, M.: Transport of dusts from East Asian and non-East Asian sources to
452 Hong Kong during dust storm related events 1996–2007, *Atmospheric Environment*, 44, 3728-3738,
453 10.1016/j.atmosenv.2010.03.034, 2010.

454 Liu, Z., Vaughan, M., Winker, D., Kittaka, C., Getzewich, B., Kuehn, R., Omar, A., Powell, K., Treppe,
455 C., and Hostetler, C.: The CALIPSO Lidar Cloud and Aerosol Discrimination: Version 2 Algorithm and

456 Initial Assessment of Performance, *Journal of Atmospheric & Oceanic Technology*, 26, 1198-1213, 2009.

457 Mikami, M., Shi, G. Y., Uno, I., Yabuki, S., Iwasaka, Y., Yasui, M., Aoki, T., Tanaka, T. Y., Kurosaki, Y.,
458 Masuda, K., Uchiyama, A., Matsuki, A., Sakai, T., Takemi, T., Nakawo, M., Seino, N., Ishizuka, M.,
459 Satake, S., Fujita, K., Hara, Y., Kai, K., Kanayama, S., Hayashi, M., Du, M., Kanai, Y., Yamada, Y.,
460 Zhang, X. Y., Shen, Z., Zhou, H., Abe, O., Nagai, T., Tsutsumi, Y., Chiba, M., and Suzuki, J.: Aeolian
461 dust experiment on climate impact: An overview of Japan–China joint project ADEC, *Global and*
462 *Planetary Change*, 52, 142-172, 10.1016/j.gloplacha.2006.03.001, 2006.

463 Omar, A. H., Winker, D. M., Vaughan, M. A., Hu, Y., Trepte, C. R., Ferrare, R. A., Lee, K.-P., Hostetler,
464 C. A., Kittaka, C., Rogers, R. R., Kuehn, R. E., and Liu, Z.: The CALIPSO Automated Aerosol
465 Classification and Lidar Ratio Selection Algorithm, *Journal of Atmospheric and Oceanic Technology*, 26,
466 1994-2014, 10.1175/2009jtech1231.1, 2009.

467 Omar, A. H., Winker, D. M., Tackett, J. L., Giles, D. M., Kar, J., Liu, Z., Vaughan, M. A., Powell, K. A.,
468 and Trepte, C. R.: CALIOP and AERONET aerosol optical depth comparisons: One size fits none,
469 *Journal of Geophysical Research: Atmospheres*, 118, 4748-4766, 10.1002/jgrd.50330, 2013.

470 Rodríguez, S., Alastuey, A., and Querol, X.: A review of methods for long term in situ characterization
471 of aerosol dust, *Aeolian Research*, 6, 55-74, 10.1016/j.aeolia.2012.07.004, 2012.

472 Rosenfeld, D., Rudich, Y., and Lahav, R.: Desert Dust Suppressing Precipitation: A Possible
473 Desertification Feedback Loop, *Proc Natl Acad Sci U S A*, 98, 5975-5980, 2001.

474 Shao, Y., Wyrwoll, K.-H., Chappell, A., Huang, J., Lin, Z., McTainsh, G. H., Mikami, M., Tanaka, T. Y.,
475 Wang, X., and Yoon, S.: Dust cycle: An emerging core theme in Earth system science, *Aeolian Research*,
476 2, 181-204, 10.1016/j.aeolia.2011.02.001, 2011.

477 Srivastava, A. K., Soni, V. K., Singh, S., Kanawade, V. P., Singh, N., Tiwari, S., and Attri, S. D.: An early
478 South Asian dust storm during March 2012 and its impacts on Indian Himalayan foothills: a case study,
479 *Sci Total Environ*, 493, 526-534, 10.1016/j.scitotenv.2014.06.024, 2014.

480 Tan, S.-C., Shi, G.-Y., and Wang, H.: Long-range transport of spring dust storms in Inner Mongolia and
481 impact on the China seas, *Atmospheric Environment*, 46, 299-308, 10.1016/j.atmosenv.2011.09.058,
482 2012.

483 Tegen, I.: Modeling the mineral dust aerosol cycle in the climate system, *Quaternary Science Reviews*,
484 22, 1821-1834, 2003.

485 Teixeira, J. C., Carvalho, A. C., Tuccella, P., Curci, G., and Rocha, A.: WRF-chem sensitivity to vertical

486 resolution during a saharan dust event, *Physics and Chemistry of the Earth, Parts A/B/C*, 94, 188-195,
487 10.1016/j.pce.2015.04.002, 2016.

488 Torres, O., Tanskanen, A., Veihelmann, B., Ahn, C., Braak, R., Bhartia, P. K., Veefkind, P., and Levelt,
489 P.: Aerosols and surface UV products from Ozone Monitoring Instrument observations: An overview,
490 *Journal of Geophysical Research*, 112, 10.1029/2007jd008809, 2007.

491 Wang, H., Zhang, L., Cao, X., Zhang, Z., and Liang, J.: A-Train satellite measurements of dust aerosol
492 distributions over northern China, *Journal of Quantitative Spectroscopy and Radiative Transfer*, 122,
493 170-179, 10.1016/j.jqsrt.2012.08.011, 2013.

494 Winker, D. M., Hunt, W. H., and McGill, M. J.: Initial performance assessment of CALIOP, *Geophysical*
495 *Research Letters*, 34, 228-262, 2007.

496 Wu, Y., Cordero, L., Gross, B., Moshary, F., and Ahmed, S.: Assessment of CALIPSO attenuated
497 backscatter and aerosol retrievals with a combined ground-based multi-wavelength lidar and
498 sunphotometer measurement, *Atmospheric Environment*, 84, 44-53, 2014.

499 Zhu, A., Ramanathan, V., Li, F., and Kim, D.: Dust plumes over the Pacific, Indian, and Atlantic oceans:
500 Climatology and radiative impact, *Journal of Geophysical Research Atmospheres*, 112, -, 2007.

501